Chemical Geology 722 (2026) 123671

Contents lists available at ScienceDirect

Chemical Geology

journal homepage: www.elsevier.com/locate/chemgeo

Research paper

Time-dependent intensity corrections for accurate quantitative point or X-ray mapping analysis by electron microprobe

Julien M. Allaz [a,*], Anette von der Handt [b,1], John J. Donovan [c]

[a] ETH Zürich, Department of Earth and Planetary Sciences, 8092 Zürich, Switzerland
[b] University of Minnesota, Minneapolis, MN 55455, United States of America
[c] Department of Geological Sciences, University of Oregon, Eugene, OR 97403, United States of America

ARTICLE INFO

Editor: Claudia Romano

Keywords:
Quantitative microanalysis
Electron probe microanalyzer
Electron beam damage
Time-dependent intensity corrections
Data accuracy
Volatile elements

ABSTRACT

Many materials undergo modifications to both structure and chemistry during electron bombardment in an electron probe microanalyzer (EPMA). This results in changes to the emitted X-ray intensities by various physical processes including heating, breaking of molecular bonds, ionization, volatilization and sputtering, subsurface static charging and subsequent mobility of the measured elements. Most of these processes are proportional to the degree and duration of electron beam exposure (analytical time, acceleration voltage, beam current, and beam focus) and to the thermal and electrical conductivity of the analyzed material. Therefore, quantitative accuracy is dependent upon correction schemes that monitor changes in X-ray emission over time, a process called Time-Dependent Intensity (TDI) corrections. This paper investigates various applications of TDI corrections and demonstrates that accurate point analyses can be obtained with such corrections. Moreover, the combination of replicate X-ray mapping with a TDI correction can produce precise and accurate quantitative element maps for beam-sensitive materials, expanding the range of materials and analytical conditions suitable for EPMA applications.

1. Introduction

Compositional change and modification of materials caused by electron bombardment has been a long-standing limitation in analysis by electron probe microanalyzer (EPMA) to achieving low detection limits, high precision and best accuracy. Examples include alkali migration in glass (Gedeon et al., 2008; Gedeon and Jurek, 2004; Jurek et al., 1998; Morgan and London, 1996; Spray and Rae, 1995), halogen migration in phosphates (Goldoff et al., 2012; Stormer et al., 1993), elemental migration in carbonates and volatilization of CO_2 (Lane and Dalton, 1994), deposition of contaminant hydrocarbons on sample surfaces during electron exposure (Hirsch et al., 1994), along with potential damage to the coating (Matthews et al., 2018).

Furthermore, the introduction of Schottky field emission electron guns (FEG) to EPMA has led to a renewed interest in low voltage analysis. The high brightness of FEG permits a significant reduction in beam size and, when a low acceleration voltage is considered ($\leq$ 5 kV), an extremely high beam energy density within a sub-micrometer electron interaction volume even at low beam currents (Saunders et al., 2014). On the contrary, a much broader beam is spread over a larger area and volume when considering a LaB_6 or W-filament at a classical 15 kV acceleration voltage with estimates of ~0.2 to 1.0 μm beam size (depending on thermoionic source, beam aperture and current), and penetration depth in the order of 1–2 μm or just under a micrometer in dense phases (e.g., monazite; Jercinovic et al., 2012). In this new and exciting analytical field, tracking and correcting for intensity changes may likely become the "new norm" for analytical protocol in order to obtain accurate data (Kearns et al., 2014; Kearns and Buse, 2016).

1.1. Time-dependent intensity changes and their corrections

Various materials have been observed to exhibit beam sensitivity, undergoing changes in the X-ray yield with time. Elastic and inelastic interactions of electrons with matter are known to cause specimen heating, electrostatic charging, atomic displacement, structural damage, sputtering, and mass loss (see review in Egerton et al., 2004). In transmission electron microscopy, it has been shown that electric fields are produced perpendicular to the beam, causing in or out motion of cations

* Corresponding author.
E-mail address: julien.allaz@eaps.ethz.ch (J.M. Allaz).
[1] Present address: The University of British Columbia, Department of Earth, Ocean and Atmospheric Sciences, Vancouver, BC, Canada.

https://doi.org/10.1016/j.chemgeo.2026.123671
Received 11 June 2026; Received in revised form 4 August 2026; Accepted 20 August 2026
Available online 22 August 2026

and anions, respectively (Jiang, 2016). Several strategies have been developed to mitigate these issues including reducing analysis count times, utilizing gentle analytical conditions such as low beam current and large beam diameter (Spray and Rae, 1995) or a higher accelerating voltage (Estour, 1971), as well as sequential analysis with cooling-off periods (Witter and Kuehner, 2004) and moving the sample during analysis, an approach called "multi-site" analysis by Fialin et al. (1999).

Discussion of beam damage effects commonly focuses on the effects of sample heating, which can be mitigated by the use of cryogenic stage (Kearns et al., 2002; Spray and Rae, 1995) or metallic sample coatings with better thermal conductivity (Allaz et al., 2020; Jercinovic et al., 2012; Kearns et al., 2014). Indeed, evidence shows that lowering the temperature of materials can reduce or mitigate the loss of light elements under electron bombardment (Nielsen and Sigurdsson, 1981; Worobiec et al., 2003) and minimize carbon contamination (Buse and Kearns, 2015). Sample cooling does not reduce the number of broken bonds, yet it prevents the migration of atoms from the irradiated area (Egerton et al., 1987).

Although all of these approaches yield net beneficial effects, they either cannot fully mitigate beam damage or are time-consuming, resulting in loss of spatial resolution, or depend on the availability of non-standard EPMA hardware such as cryogenic stages. Therefore, the focus has shifted toward data correction rather than beam damage mitigation approaches, notably through time-dependent intensity (TDI) corrections. This correction method was originally developed by Nielsen and Sigurdsson (1981) and involved the acquisition of peak X-ray intensities at discrete time intervals over the analytical interval to determine the intensity of the emission line at time-zero, when the analysis starts.

1.2. Causes of X-ray intensity changes over time

Understanding the underlying physics that leads to beam damage and changes in X-ray intensity aids in predicting, mitigating, and adequately applying the corrections required. Fig. 1 summarizes the various processes involved.

First, heat is generated by the inelastic interaction of electrons with ions and partly leads to beam damage (Egerton et al., 2004). Despite the strong control that temperature exerts (Fakhfakh et al., 2012b), it cannot be the sole cause of the TDI effect (Egerton et al., 2004; Gedeon and Jurek, 2004). Jiang and Spence (2011) empirically and theoretically show that effects from electron bombardment are different from their thermal annealing counterparts.

Another effect is sample charging at depth or surface. Surface charging is usually mitigated by the application of a metallic coating (typically 20 nm carbon) and will help dissipate the heat to some extent. However, this coating can be damaged by electron beam sputtering, which would cause additional charging issues (Matthews et al., 2018). When a primary electron beam interacts with an insulator, an electric field is created within the interaction volume, and with inelastic electron scattering it causes bonds to break, forcing migration of ions (Gedeon et al., 2008; Gedeon et al., 2000; Hughes et al., 2019; Jiang, 2016; Spray and Rae, 1995) and induces changes in element valence such as Fe and S (Hughes et al., 2020). Moreover, subsurface charging can lead to a deceleration of the electrons and hence excitation at lower beam energies (Bastin and Heijligers, 2004). A reduction in beam energy tends to yield lower X-ray intensities as the overvoltage is reduced. The opposite is true for soft X-rays (< 2 keV) as an optimum overvoltage is reached and yields a maximum X-ray production near the surface (lower absorption). Monte Carlo models show that distribution of the charge field

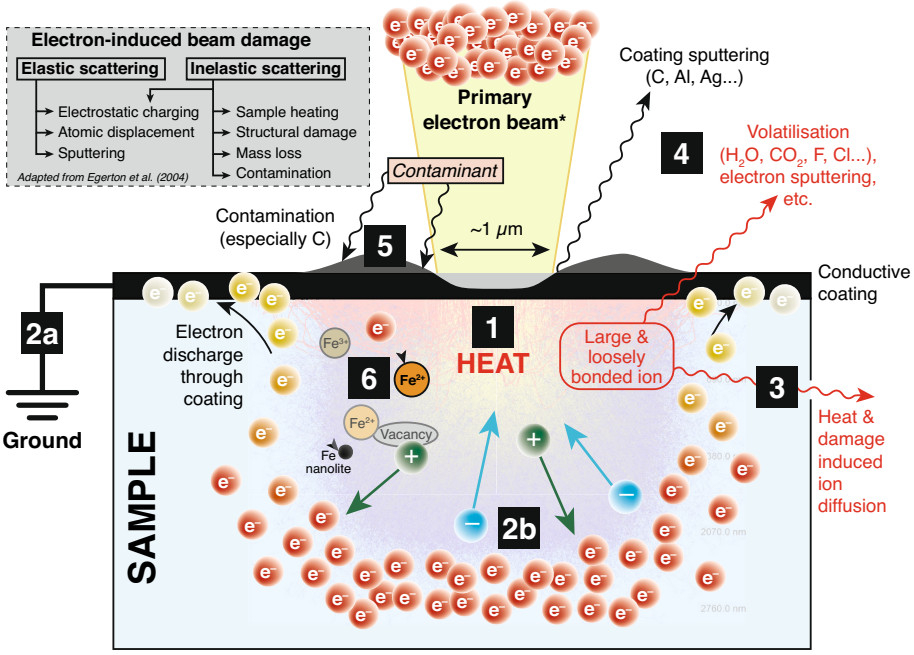

Fig. 1. Schematic cross-section of electron interactions within a beam-sensitive and non-conductive sample, such as an alkali-rich silicate glass with additional anions (F, Cl). Multiple processes can occur (e.g., Egerton et al., 2004), including (1) sample heating from inelastic interactions, (2) sample charging that is (2a) ideally mitigated by the conductive coating or (2b) potentially accumulating in the sample subsurface and causing ion migration (Jiang, 2016), (3) migration of large cations following the break-up of loose bonds by inelastic scattering and displacement of atoms by elastic scattering, (4) sputtering of loosely bound elements or compounds from the material (typically volatile such as CO_2 and H_2O), and sputtering of the conductive coating (Matthews et al., 2018), (5) contamination, especially of carbon, on and around the electron beam (Buse and Kearns, 2015), and (6) possible changes in element valence through donation of a free-electron (reduction) or formation of Fe-nanolite (magnetite or hematite) following the creation of a cation vacancy (Hughes et al., 2020). Not represented in this figure is the deceleration of primary electrons due to subsurface charging, breaking of atomic bonds through inelastic scattering, and the displacement of atoms due to elastic scattering (Egerton et al., 2004). Background image is a Casino Monte Carlo electron trajectory simulation in NIST SRM® 610 glass at 15 kV assuming a 1 μm beam diameter (i.e., a typical condition with a W electron gun). Much smaller beam size and interaction volumes are expected with FEG at lower acceleration voltage, amplifying further the depicted effects as the same energy is concentrated in a smaller analytical volume.

is shifted toward the surface in high average Z matrices due to the higher elastic scattering, while lower average Z matrices allow deeper penetration of the electrons (Gedeon et al., 1998; Jbara et al., 1997). However, lower average Z matrices are more sensitive to a particular electrical field (Gedeon et al., 1998).

In general, the shape of the X-ray intensity decay over time depends on the electron dose, the chemical composition of the irradiated material, the sample thermal conductivity and the ion mobility (Morgan and London, 1996). As the heat and electric field develops within a material, ions start migrating which can lead to a local change in material composition and enhance or decrease certain X-ray production. These effects will unavoidably result in a change over time in shape of the $\phi(\rho z)$ curve that describes the mass-depth distribution of X-ray generation (Bastin and Heijligers, 2004; Gedeon et al., 1998; Jbara et al., 1997). Finally, changes in X-ray intensity over time can be further complicated by crystallographic orientation effects in anisotropic minerals where crystal lattice orientations exhibit different behavior under the beam (e.g. apatite, phyllosilicate; Goldoff et al., 2012; Morgan and London, 1996; Stormer et al., 1993).

All these combined effects lead to a highly variable response of each material to the radiation damage. Therefore, application of correction factors estimated on similar materials from the literature can yield erroneous results. Changes in X-ray intensity over time are best tracked empirically during acquisition and should be corrected for as necessary on a point by point or pixel by pixel basis. Some X-ray intensities in beam-sensitive materials may show a positive or negative change over time as a function of time, leading to over- or underestimation of the quantity, respectively. In order to get accurate data, the analyst needs to know the expected X-ray intensity at zero elapsed time. As this is not physically possible, very short count times are often suggested for the analysis of volatile elements especially in the absence of other correction options (Spray and Rae, 1995). The downside of this approach are the limitations it imposes on the achievable precision and detectability on a given analysis spot.

2. Methods

EPMA measurements were performed on five distinct electron microprobes: the Cameca SX100 at the CAMCOR shared-user facility at the University of Oregon (USA), the JEOL JXA-8900R and JXA-8530FPlus at the Department of Earth Sciences, University of Minnesota (USA), the JEOL JXA-iHP200F at the University of British Columbia (Canada), and the JEOL JXA-8200 and JXA-8230 at ETH Zürich (Switzerland). All instruments are equipped with their dedicated Cameca or JEOL software. All data were processed with the third-party software *Probe for EPMA* (PFE) from Probe Software, Inc. Analytical conditions were typically 15 to 20 kV acceleration voltage and beam currents were regulated from 0.5 to 200 nA in tests performed on various beam-sensitive glass and mineral samples.

Empirical solutions for the analysis of beam-sensitive materials known as time-dependent intensity (TDI) corrections were implemented in PFE and related software, notably *ProbeImage* for map acquisition and *CalcImage* for quantification of X-ray element maps. Sadly, aside from a rudimentary sub interval measurement for point analysis in the Cameca software, no equivalent is found in the original Cameca or JEOL programs, and users have to perform their own TDI corrections in post-processing or find another third-party software such as *MigrationCorrection* from McSwiggen & Associates, Inc. The latter allows JEOL users to collect a series of element measurements and then extrapolate X-ray intensities back to time-zero. The corrected count rates are then written into the analysis files and re-processed through this software. Unfortunately, such simple correction routine neglects a re-correction of the matrix effects from the modified intensities as discussed below. An alternative approach uses a set of correction factors obtained on a material of similar composition to the unknown in order to correct for the expected intensity changes in some elements, such as alkalis in glass (e.g., Koepke et al., 2004). Regardless of the choice of software or method that provides TDI corrections, it is crucial to apply intensity corrections before matrix corrections and not in post-processing to obtain accurate quantitative results (Spray and Rae, 1995).

3. X-ray intensity changes in EPMA

In the following section we analyzed several glass and mineral reference materials and natural geological samples to explore the effects of electron bombardment during EPMA analysis and the associated changes in X-ray intensities. Conventionally, it has been assumed that the emission intensity decay is exponential (Nielsen and Sigurdsson, 1981). However, for extreme cases of radiation damage such as alkali rich or hydrous glasses, we can observe hyper-exponential and even double-exponential decay curves.

3.1. Na-rich synthetic glass

We first consider a series of TDI acquisitions of Si Kα, Na Kα, Ca Kα and K Kα obtained on a JEOL JXA-8200 at 15 kV, variable beam size (focused to 20 μm) and beam current (0.5 to 50 nA) in Na-rich NIST SRM® 610 glass to illustrate this effect (Fig. 2). Each analysis included 30 × 10 s intervals counting on peak only for a total analysis time of ~450 s including a ~ 4 to 5 s latency between each sub-interval measurement on this old instrument, and maybe ~1 to 2 s on newer machines. Four to five analyses were repeated for each condition considered. When a large beam size and low current is applied (10 μm; 1 nA), the correction is unnecessary for some elements (e.g., for Ca Kα in Fig. 2a), whereas it follows a natural logarithm trend over linear time for Si Kα (ln-linear; Fig. 2b) and a hyper-exponential trend for Na Kα (Fig. 2c) when a smaller beam of 5 μm is used. Double-natural-logarithm (ln−ln) correction is sometimes required at higher dose (e.g., Si Kα at 20 nA and 10 μm; Fig. 2d) and can yield spurious results. At very high dose, the effect is too strong to be corrected (e.g., Si and Na Kα at 50 nA and focused beam; Fig. 2e,f). At times the curves also exhibit oscillating behavior with large or small amplitudes.

At very low beam energy densities, the TDI curve starts out as a flat plateau followed by a progressive change in slope (Fig. 3). This "incubation" period tends to occur when the sample thermal conductivity is relatively high and the electron dose densities are relatively low (Gedeon et al., 2000). NIST 610 glass has a thermal conductivity of 0.7 [W/m·K] (Holá et al., 2018) and the temperature rise within the analyzed volume considering a ~ 1 μm beam diameter at 15 kV acceleration voltage is estimated to be ~5 to ~510 °C at 0.5 to 50 nA using eq. 3.196 of Reimer (1998; p. 118). Increasing the beam diameter helps to dissipate the heat to the inverse of the beam radius. The delayed temperature increase of the sample, which stimulates charge trapping and ion migration causes the onset of ion migration to be delayed relative to the TDI interval (Fakhfakh et al., 2012a; Jurek et al., 1998). It also coincides with the stabilization of the absorbed current coming out of the sample, which could be ascribed as a "charging time" for the building of the electric field within the sample. The length of the incubation delay is composition-dependent and generally longer for the larger alkali ion sizes in alkali-rich glasses (Gedeon et al., 2000). We sometimes observe that the first spot analysis is affected the most as the sample area is still "cold", while subsequent analysis points in the vicinity often show a more reduced effect. Materials that exhibit an incubation delay of several seconds before the onset of element migration or contamination or incur beam damage dominantly in the first few seconds are difficult-to-fit decay curves (Morgan and London, 1996). For instance, a fourth-order polynomial is required to fit the example provided in Fig. 3.

The overall damage test in this glass is evaluated with all 21 TDI acquisitions at variable current and beam size (0.5 to 20 nA and focused beam to 20 μm; Fig. 4). Results depict the change of X-ray intensity in counts per second per nanoamp (cps/nA) over the total beam energy

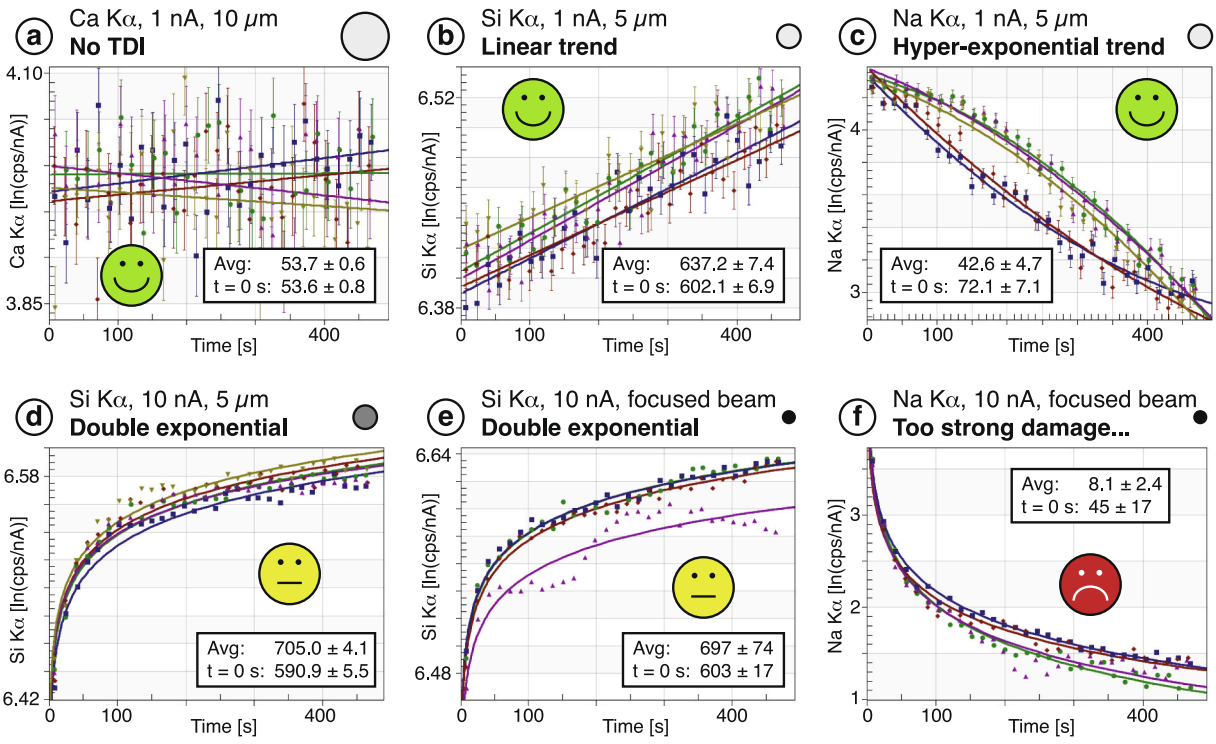

Fig. 2. Examples of different TDI trends observed in Na-rich NIST SRM® 610 glass, shown as time versus cps/nA in natural logarithm (ln) scale. All data were acquired at 15 kV on a JEOL JXA-8200 (W-filament). This glass has a nominal composition of 72 wt% SiO_2, 14 wt% Na_2O, 12 wt% CaO and 2 wt% Al_2O_3. Summed average (Avg) and intercept ($t = 0$ s) of the fitting curve given in each plot as cps/nA with 1 standard deviation of the repetition of 5 analyses. Based on the lowest beam damage data, an accurate intensity on the instrument considered is ~54 cps/nA for Ca Kα, ~603 for Si Kα and ~ 72 for Na Kα. Uncertainty on each measurement point is shown at 1σ level in (a-c) and it is smaller than the plot symbols in (d-f). (a) No significant trend for Ca Kα at 1 nA and 10 μm, (b) log-linear correction on Si Kα and (c) hyper-exponential correction on Na Kα at 1 nA and 5 μm, (d) double-exponential correction on Si Kα at 10 nA and 5 μm, (e) strong double-exponential correction at 10 nA and 5 μm with an acceptable yet imprecise intercept on Si Kα and (f) an inaccurate intercept for Na Kα due to excessive damage.

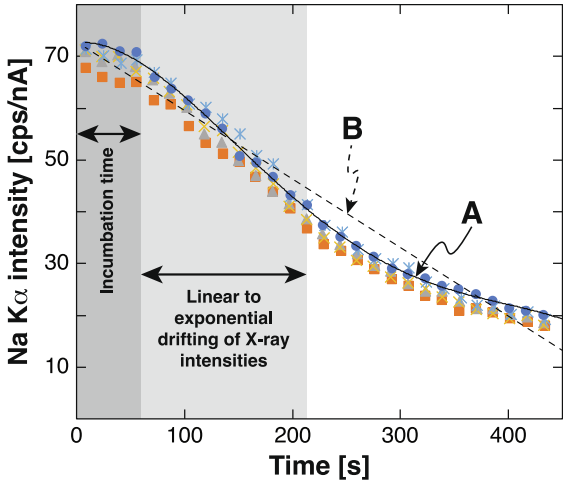

Fig. 3. TDI acquisitions for 4 analyses of Na Kα at 15 kV, 10 nA, and 20 μm beam size in NIST 610 glass. An incubation effect causes difficulties for curve fitting, requiring in this case a 4th-order polynomial fitting. Fitting on blue dots: (A) 4th order, $y = -5{\cdot}10^{-9}{\cdot}x^4 + 5{\cdot}10^{-6}{\cdot}x^3 - 1.7{\cdot}10^{-3}{\cdot}x^2 + 1.48{\cdot}10^{-2}{\cdot}x + 72.69$ ($R^2 = 0.9989$); (B) linear, $y = -0.132{\cdot}x + 72.76$ ($R^2 = 0.9612$). (For interpretation of the references to colour in this figure legend, the reader is referred to the web version of this article.)

density in mJ/μm^2, the latter being the product of the acceleration voltage (in kV), the beam current (in μA) and the analysis time (in s) divided by the impacted area (in μm^2). Normalization to the analyzed volume instead of the surface would certainly be more adequate, yet complicated as it would necessitate the use of Monte Carlo simulations to reveal the electron interaction volume and to calculate the electron energy loss across this volume. Such simulations would further require knowledge of the sample composition and density; it would thus require an iterative and more complex approach than simply considering the impacted surface. The incubation period becomes clearer and seems to require in this material an energy load of ~0.04 mJ/μm^2. Beyond this point, X-ray intensity change follows an almost linear change (up to ~0.1 mJ/μm^2) becoming exponential to hyper-exponential and presents a change in slope around 0.3 mJ/μm^2. At higher beam energy densities, a more chaotic behavior might be expected and could become difficult to model. Finally, it should be noted that K is only reported as uncertified trace amount in this NIST 610 glass at 461 ppm, and the TDI trend for this element essentially reflect the change in bremsstrahlung intensity over time at this X-ray wavelength. This change thus reflects a change in the overall material composition and structure.

3.2. *Modes of TDI acquisition*

Two different modes of TDI data acquisitions are available in PFE for spot analysis that have different advantages depending on the application: "assigned-calibration" time-dependent intensity (AC-TDI) and "self-calibration" TDI (SC-TDI) calibration. In the AC-TDI method, the TDI intensity decay curve will be calibrated precisely on an unknown sample for each element and can then be assigned to some or all subsequent analyses. The important assumption is that the TDI behavior of all analyzed X-rays on the first analysis point used for calibration are similar to the unknowns to be analyzed. This approach is advantageous when long acquisition times are required and the TDI behavior of the material is unlikely to change or the user wants to isolate sample

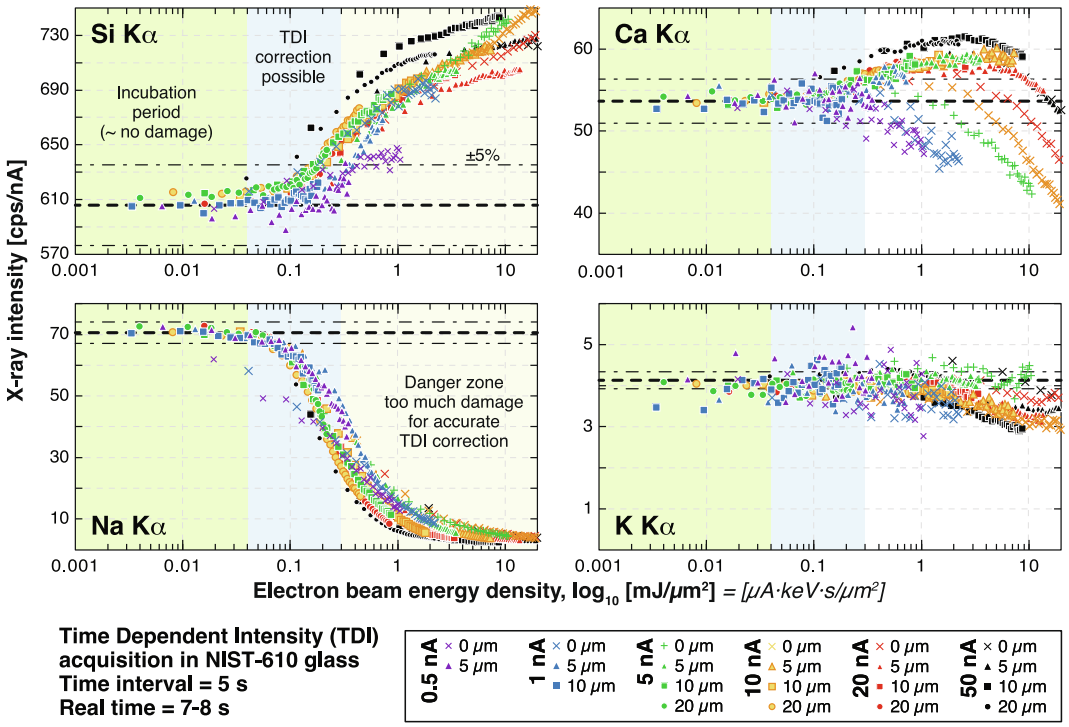

Fig. 4. Complete set of TDI tests in NIST SRM® glass 610 for (a) Si Kα, (b) Na Kα, (c) Ca Kα, and (d) K Kα, using the supplementary data from Allaz et al. (2026). The overall change is essentially a function of the total beam energy density expressed as millijoule per square micrometer (mJ /μm^2 = keV·μA·s/μm^2). The nominal beam size and beam current are given. Beam size on the instrument used was calibrated with the largest beam aperture (#1), whereas aperture #2 was used. We observed and considered for the calculation a 30% reduction in beam size compared to the nominal beam size at aperture #1, as confirmed by observation of beam damage spots and as specified in the JEOL EPMA manual. For the focused beam condition (0 μm), the impacted area was assumed to reflect the expression of the electron interaction volume at the surface, which would be a diameter of ~2 μm (see Fig. 1). All numerical data are available in the Supplementary Table 1.

precision from TDI precision. Examples include monazite dating with multiple analyses in a single chemically homogeneous domain, or traverses along a single mineral grain. Because a consistent TDI correction is used for all points or pixels, data should reflect real differences in composition (or volatilization) rather than the variance of individual (SC-) TDI corrections.

The SC-TDI acquisition method instead utilizes a separate TDI acquisition on each analysis point. For the first element analyzed on each wavelength dispersive spectrometer, the TDI correction is evaluated during the post-processing and is activated or not. If the TDI correction is deactivated for an element, the total sum of X-ray counts of all TDI intervals are utilized, otherwise, the TDI slope of every point measurement is applied to the summed intensities of each point measurement. This method works well when samples have variable compositions or that the TDI effect is known to be dependent on grain orientation.

To further refine the TDI technique and facilitate the analysis of the most beam-sensitive materials, one can combine the TDI correction approach with quantitative element mapping in what we call "TDI scanning". The TDI scanning principle entails the acquisition of several (> 3 to 5) sequential fast beam or stage scanning X-ray maps (Fig. 5). These replicate X-ray maps can be acquired automatically with *ProbeImage*, corrected for TDI effects and transformed into fully quantitative element maps through *CalcImage* software. Other advanced quantitative map processing options include a logarithmic dead time correction for mapping at high count rates (Donovan et al., 2023), the mean atomic number (MAN) background correction (Donovan et al., 2016; Donovan and Tingle, 1996), modern mass absorption coefficients (Chantler et al., 2005), enhanced interference and blank corrections (Donovan et al., 2011; Donovan et al., 1993). Ultimately, an accurate quantitative analysis on a pixel-by-pixel basis is obtained (Donovan et al., 2021), and precise analyses can ultimately be extracted by averaging multiple

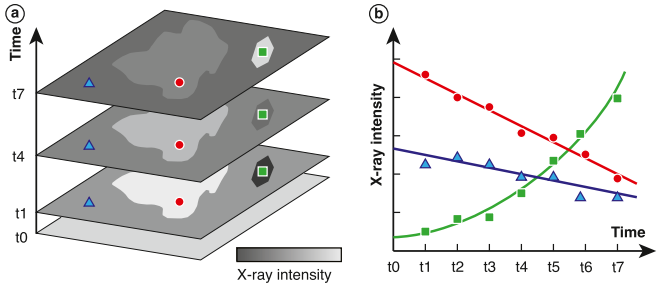

Fig. 5. Principle of "TDI scanning" correction for X-ray intensity maps. (a) A multi-phase area is mapped several times at certain dwell time (t1, t2, t3…). (b) TDI curves are obtained by comparing X-ray intensities at each time-stamped map pixel acquisition for each individual analyzed X-ray.

pixels from the TDI corrected maps, as we will demonstrate below.

During X-ray mapping, either in beam scanning or stage mapping mode, the electron beam dwells for merely 0.01 to 0.1 s or more on a given pixel position, thereby mitigating beam damage from extended temperature increases and subsurface charging. Acquisition of a series of sequential mapping passes over the same area allows tracking of the X-ray intensity changes for each pixel, while improving counting statistics and precision as needed. This method shares characteristics with the recommendation of analyzing in beam-raster mode (Spray and Rae, 1995), but provides much better control on spatial and temporal variabilities.

3.3. Processing of TDI curves

Since X-ray counting is a time integrated method where the count rate multiplied by the integration time equals the total photons

measured, any TDI correction must utilize both the summed X-ray intensities and the TDI slope as determined from interval measurements. The typical procedure is to determine the shape of the decay curve over time (linear, natural logarithm, hyper-exponential, etc.) and by subtraction of the regression slope at one half the time integration arrive at the ideal emission intensity at time-zero, prior to the beam damage (Fig. 6). The correction can be either positive or negative if the X-ray intensity decreases or increases, respectively, and can show concave up or down shape.

Different mathematical models can be applied to the acquired TDI curves. In particular, log natural – linear, hyper-exponential, and double-exponential extrapolations (Fig. 2) are currently available within the PFE to fit the empirical decay curves while other software solutions currently offer only linear fits. The log natural - linear TDI fit is calculated as:

$$I_{TDI\ (ln-linear)} = exp\left[\ln(I_{raw}) - a\cdot\frac{t}{2}\right]$$

where t is the elapsed time and a is the slope of the linear regression in log natural (ln) space. The hyper-exponential TDI fit is calculated as:

$$I_{TDI\ (hyper-exp)} = exp\left[\ln(I_{raw}) - a\cdot\frac{t}{2} - b\cdot\left(\frac{t}{2}\right)^2\right]$$

where t is the elapsed time and a is the slope of the linear regression and b is the 2nd derivative in log natural space. Finally, the double-exponential fit is calculated as:

$$I_{TDI\ (double-exp)} = exp\left[\ln(I_{raw}) - a\cdot\ln\left(\frac{t}{2}\right)\right]$$

where t is the elapsed time and a is the slope of the linear regression in double log natural space.

3.4. The importance of TDI for matrix correction procedures

Accurate determination of X-ray intensities before applying the matrix corrections is necessary to obtain accurate results (Spray and Rae, 1995). In the data correction scheme, any TDI correction should occur before any peak interference corrections, background corrections, and calculation of missing elements. All elements are then processed together through the matrix correction scheme (Fig. 7).

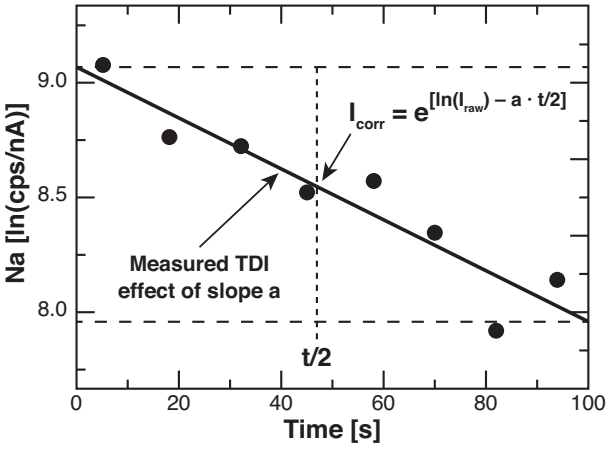

Fig. 6. Schematic of TDI corrections, utilizing geometric fits to X-ray intensity data acquired at even time intervals. The slope of the decay curve is utilized rather than the time-zero intercept, providing a more robust regression when utilizing the AC-TDI method where individual points can vary in average intensity.

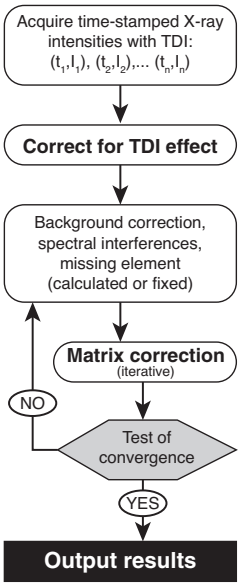

Fig. 7. Flow chart illustrating the TDI correction prior to background, spectral interference and most importantly, the iterative matrix corrections.

3.5. Accuracy and precision with TDI corrections

The accuracy of the TDI correction is entirely dependent on the ability to fit the decay curve accurately. As seen with the Na-rich NIST 610 glass, the analyst visually assesses the change and opts for a ln-linear, hyper-exponential, or double-ln correction in order to obtain a best fit to the TDI points depending on the magnitude of the change of X-ray intensity over time (e.g., Fig. 2f). Inaccurate regressions may cause accuracy errors due to either over-extrapolation or under-extrapolation. A bad fit can be due to (a) the existence of an incubation period, (b) an inaccurate recording of the time of each TDI interval, (c) an excessively high beam energy density rendering the first TDI point already inaccurate, or (d) not enough intervals or too many intervals.

The problem of a possible “incubation” period (e.g., Fig. 3) can be mitigated by either choosing a beam energy density that is neither too “cold” nor too “hot” or not having too many total intervals included to avoid the strong damage zone (i.e., pass the change in decay slope; Fig. 3). In this particular case, a linear regression may result in a better estimation of the time-zero intensity, even though the R^2 fit statistics for a linear fit are somewhat worse (Fig. 3, fitting B). Alternatively and counterintuitively, one might want to add a short delay or increase the total electron beam energy density by increasing beam current or decreasing the beam diameter so that the sample is more rapidly heated, resulting in a linear TDI trend ion migration regime with the first interval covering the incubation period. However, this latter approach has to be carefully moderated as too much electron dose density will create ion migration effects that rapidly become excessively large, resulting in accuracy errors when extrapolating to time-zero or when determining the slope and curvature (e.g., Fig. 2d-f).

The second issue about the accuracy of time stamping of data is depending on hardware and software response times. If incorrect, it can affect the TDI curve shapes. Morgan and London (2005) found multiple potential causes for such delays, including stabilizing the counting circuitry and time for moving the spectrometers to the X-ray peak position. Additional software delays between sending a command, counting, and returning the result for each interval are unavoidable. PFE records any delay after electron beam exposure and the starting of X-ray counting as well as the time between interval acquisition in real time relative to the removal of the Faraday cup. Nevertheless, TDI acquisition should be tested to track and address any hardware or software problems that can significantly delay data acquisition. Note that anomalous low X-ray

intensities can notably occur in the first TDI interval when using very short interval times (≤1 s) on JEOL microprobes if the Faraday cup out delay is not sufficiently long.

The use of TDI counting also affects the precision of the analysis, as the fitting of each short-time interval, for instance 5 intervals of 6 s, has worse counting statistics than a single 30-s-long acquisition due to regression of noisier subinterval intensities. An ideal time-interval should be chosen to enable sufficient counting statistics depending on the required analytical sensitivity, and this optimum might vary depending on the analyzed X-ray and the chosen wavelength dispersive spectrometer, and ultimately the expected count rate for this X-ray and its collection efficiency. If the statistics are too poor, and the analyzed X-ray does not show a significant drift in intensity, unnecessary imprecision is added in the analysis as a consequence of fitting noisy data and applying that to the summed intensities (e.g., Fig. 2a). In the case of beam stable elements, the average intensity over the total analysis time should be considered rather than the TDI-corrected count rate.

This measurement problem is like "finding the Goldilocks zone" and has no universal answer. For a given sample, some electron beam conditions might be acceptable for one mineral composition and a specific orientation, but not for the other. The Goldilocks zone will not only be determined by the material properties (and sometime orientation), but also by sample coating type and thickness. Therefore, it is best to test empirically the sample resilience to electron beam at the desired conditions (beam voltage, current, and size, coating, etc.), in order to determine the maximum counting time prior to a too strong damage (e.g., beyond ~0.3 mJ/μm^2 in NIST 610 glass; Fig. 4). Once this time is determined, an adequate time interval is chosen to reach a decent statistics on each time interval. Examples from the literature include a maximum dose of ~10.5 mJ/μm^2 in apatite coated with ~12 nm Al + 6 nm C and merely 0.5 mJ/μm^2 when only 20 nm C coating is considered (Allaz et al., 2019), and natural albite standard at ~4 to 6 mJ/μm^2 (Allaz et al., 2023). The analyst should still avoid too high beam energy densities, otherwise the TDI correction will return erratic results. For instance, any measurement of NIST 610 glass using a focused beam and ≥ 10 nA will result in an uncorrectable result as the first TDI intervals are already inaccurate (Fig. 2e,f).

We test precision and accuracy by running point analyses in NIST 610 glass, at various beam conditions that result in a total of ≤0.25 mJ/μm^2 (Fig. 8). Without a TDI correction, all acquisitions obtained by summing 9 time-intervals yield highly inaccurate results. With hyper-exponential TDI correction, results are very close to the nominal matrix glass composition of this material, especially for analyses run at 1 nA and focused beam, at 5 nA and 5 μm beam size, or at 10 nA and 20 μm. It should be noted that the composition from NIST is normalized to 100%, whereas ~1 wt% of trace elements are present in this glass (or ~ 1.5 wt % in oxide form). Thus, each reference wt% value should be decreased by 1 to 1.5% (Fig. 8). When 18 time-intervals are considered instead of 9 (light-colored points; Fig. 8), the TDI-corrected results tend to be inaccurate with lower SiO_2 and more variable for Na_2O even. On the system considered for these tests (JEOL JXA-8230), the software required ~1 to 2 s extra time at each time interval to retrieve, store, and continue counting. Thus, the acquisition with 18 intervals took more time, and yielded a higher beam damage and slightly worse accuracy (blue diamonds in Fig. 8).

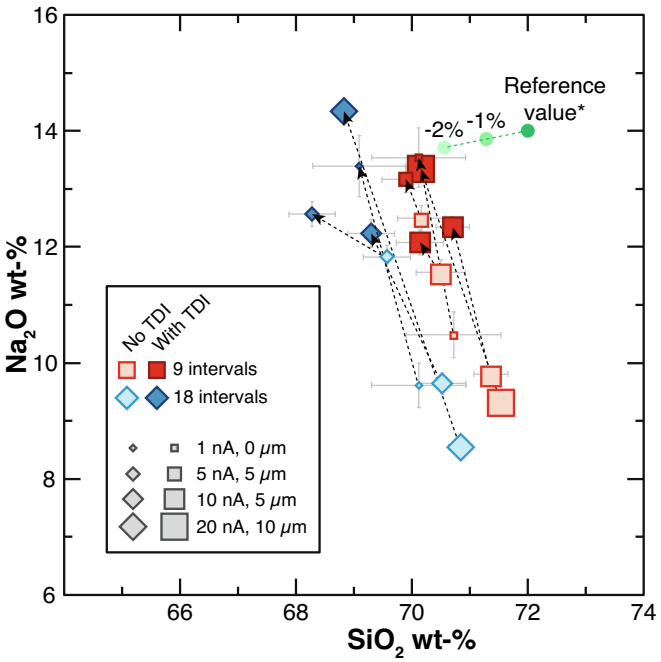

Fig. 8. Weight-% results of SiO_2 versus Na_2O in NIST SRM® 610 at 15 kV and variable beam size (0, 5, and 10 μm) and beam current (1, 5, 10, and 20 nA). Each analysis point is an average of 10 repetitions; thin gray lines are 2σ standard deviation. Each analysis yielded a total electron beam density of ~0.2 to 0.25 mJ/μm^2, however analyses with 18 intervals have a much longer latency time (+30 s; compared to an additional +16 s with 9 intervals). See Supplementary Table 2 for detailed analytical setup and numerical results with or without TDI on each point.
* The nominal NIST 610 glass matrix composition is normalized to 100%, yet there is ~1 wt% of trace elements, or ~1.5 wt% in oxide form.

4. Applications and examples of TDI correction effects

4.1. Alkali-rich glasses

Accurate and precise analysis of alkali-rich glasses is a common concern in the Earth science community and material science. For example, an inter-comparison study carried out by 24 different analytical laboratories shows the challenges in obtaining accurate sodium concentrations in tephra (Kuehn et al., 2011). Glass structures facilitate alkali ion migration compared to mineral structures and the structural environment of Na has been shown to influence its migratory behavior. In particular, Morgan and London (1996) demonstrated a change for the role of Na from being a charge-balancing cation to a hydrolyzed complex in hydrated samples. Migration in alkali glasses has been shown to be most pronounced for Na and K and impeded by the presence of Ca, Al, Mg and Fe (Vassamillet and Caldwell, 1969). As shown with Na-rich NIST 610 glass, the trend is mostly a function of the beam energy density (Fig. 4), or simply a function of time for a fixed voltage, current, and beam size. Alkali ions in glass are preferentially released from their sites with assistance from the heat generated by inelastic collisions, the elastic scattering causing atomic displacement. This diffusion is possibly further influenced by the sub-surface charging. Consequently, the ions are driven by the electric field toward the bulk of the irradiated sample (Fig. 1). Hence, alkali ions are able to migrate long distances and finally accumulate at the bottom of the irradiated volume becoming immobile, or diffuse sideways out of the interaction volume.

Very alkali-rich or hydrous glasses experience the majority of beam damage in the first few seconds of analysis at low beam energy density (e.g., ~0.04 mJ/μm^2 in NIST 610 glass), making tracking of TDI curves difficult due to the limitations of detector electronics. Such materials are better analyzed using the TDI scanning approach to reduce the irradiation time on a given spot and thereby minimize beam damage as much as possible. Better precision can then be obtained by averaging multiple TDI-corrected pixels. This is further shown in Fig. 9 with accurate concentrations obtained in the beam-sensitive Corning Archeological Reference Glass 'A' using the TDI scanning approach (Vicenzi et al., 2002).

Eleven consecutive maps were combined and corrected for TDI change over time and quantified with standards and matrix correction. Analyses extracted from the maps are reported under Fig. 9 to show the improvement on data accuracy when TDI correction is considered.

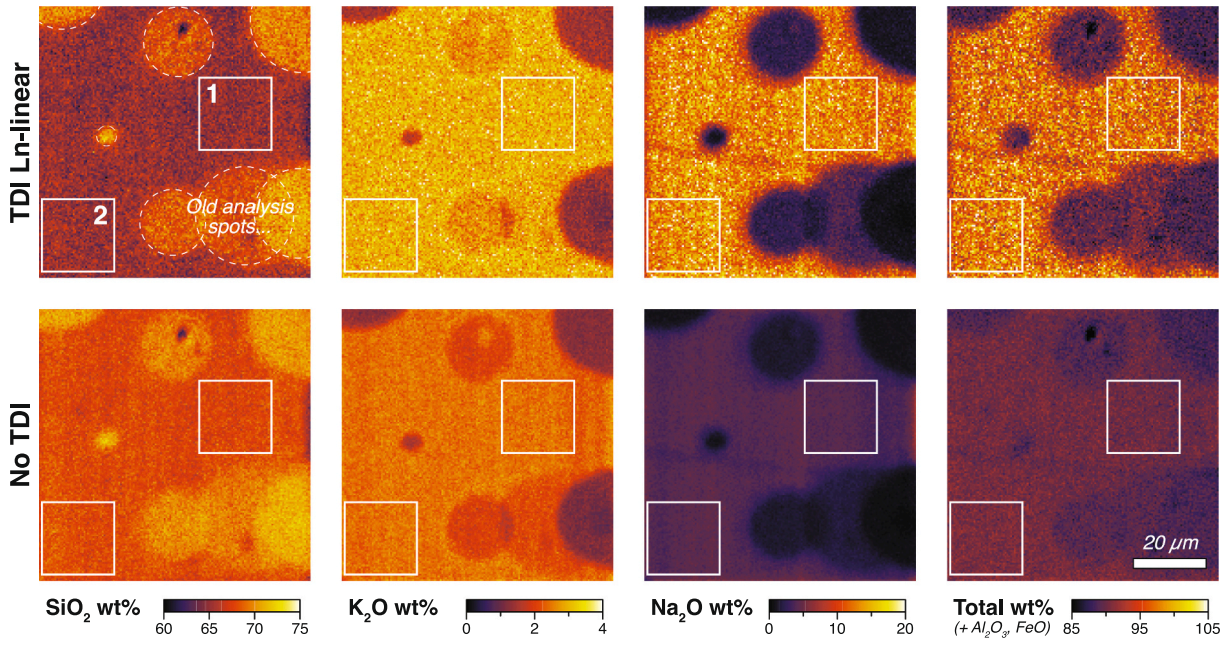

Corning A-glass
JEOL-8900
(U. Minnesota)
Analytical conditions
15 keV, 30 nA, focused,
0.5 µm/px, 50 ms/px
11 TDI map repetitions

	SiO_2	Al_2O_3	K_2O	Na_2O	Fe_2O_3	Total*
Area 1 + TDI	**65.11(6)**	0.985(9)	**2.989(16)**	**13.22(13)**	1.100(14)	97.18(16)
Area 2 + TDI	**65.29(6)**	0.977(9)	**2.961(16)**	**13.59(14)**	1.130(15)	97.72(16)
Area 1	**67.80(4)**	0.998(5)	**2.431(8)**	**3.91(2)**	1.129(8)	90.05(4)
Area 2	**68.15(4)**	0.991(3)	**2.441(8)**	**4.15(2)**	1.150(8)	90.66(4)
Ref.	*66.56*	*1.00*	*2.87*	*14.3*	*1.09*	*100*

*Weight-% (1σ std error). *Totals for maps and reference values include trace elements from Vicenzi et al. (2002).*

Fig. 9. Quantitative X-ray maps for SiO_2, K_2O, Na_2O and analytical total in wt% in Corning "Glass A" reference material with and without TDI correction applied. Quantitative analyses are extracted from two 40 × 40 pixel areas, corresponding to a total of 880 s of analysis for 11 repetitions of maps acquired at 0.05 s per pixel. All missing oxides above 0.01 wt% listed in Vicenzi et al. (2002) were considered as specified elements during matrix correction and data processing. Brighter or darker round spots on maps are previous analysis points that lead to variable and permanent alkali depletion in the material and related gain in Si. Matrix tables of all analyzed elements and with or without TDI are available in the Supplementary Table 3.

Although not perfect, the TDI-corrected maps are significantly more accurate than the results without TDI correction and in agreement with the published values of Vicenzi et al. (2002). Without TDI correction, the loss of Na_2O (−70%) and K_2O (−18%) is clear on both analyses. However, the effect on minor elements Al and Fe remains minimal, and accumulated data should be considered for those elements. TDI scanning yields good results making this an ideal application for the most beam-sensitive materials or small or irregularly shaped materials.

Melt, especially when hosted and geochemically shielded by a host mineral, is crucial and important to record the evolution of the magmatic conditions. One common application of EPMA in the Earth sciences is the study of melt inclusions. Melt inclusions are typically small (< 10–20 µm), can have complex architecture with gas bubbles and commonly contain high concentrations of alkalis and volatile elements (e.g., H_2O, CO_2, F, Cl), some of them being not analyzable by EPMA (e.g., H) or with difficulty (e.g., C, O). Water is commonly determined by difference to the expected 100 wt% total. Hughes et al. (2019) demonstrated that careful correction for TDI effects as well as correcting for subsurface charging using reference material of known volatile composition can yield ±0.1 wt% accurate results with EPMA in hydrous glasses, providing that suitable, in addition to TDI correction, secondary reference materials of known water content are considered.

We investigated the main composition of a rhyolitic melt inclusion through TDI scanning (Fig. 10). The application of TDI scanning generally provides better results over TDI corrected spot analyses. First, TDI scanning reveals small features within the melt inclusion (e.g., cracks, inclusions) that would likely have been included in a spot analysis, especially when using a defocused beam, but can be avoided when extracting compositions selectively from the map. TDI corrected maps reveals also higher Na_2O and K_2O contents and hence lower calculated H_2O contents relative to the uncorrected values. Notably, correction factors of up to −250% and − 75% are observed for Na_2O and K_2O, respectively. The shorter pixel dwell times achieved in mapping mode compared to the minimum TDI time intervals in spot acquisition mode allow for a more detailed analysis of the decay curve during the initial stages of beam exposure. This is particularly crucial for materials that experience varying levels of beam damage within the first seconds of analysis. While X-ray maps exhibit an unusual grid patterning, potentially due to trailing charge effects from a non-stationary beam in an insulator, TDI correction resolves this analytical artifact as well.

4.2. Carbonate minerals

Another classical example of beam-sensitive material are carbonate minerals (Ca, Mg, Fe, Mn, Sr…)CO_3. Through beam damage, they tend to degrade and CO_2 is volatilized. It commonly results in an increase in X-ray intensity of the remaining cations, especially Ca. This damage can be also visible on the primary standard material used, and thus the TDI correction should always be applied on both standards and unknowns (Fig. 11). With the help of TDI scanning, a considerable gain in data quality and accuracy of major element analysis is obtained, as shown in the element mapping of a natural Mg-bearing calcite (Fig. 12). If the analyst scans a carbonate without a TDI correction, the final results will yield too high analytical totals when recalculating CO_2 by stoichiometry, with variable effect on different grains. On the contrary, a TDI corrected map yields more accurate results, with results approaching

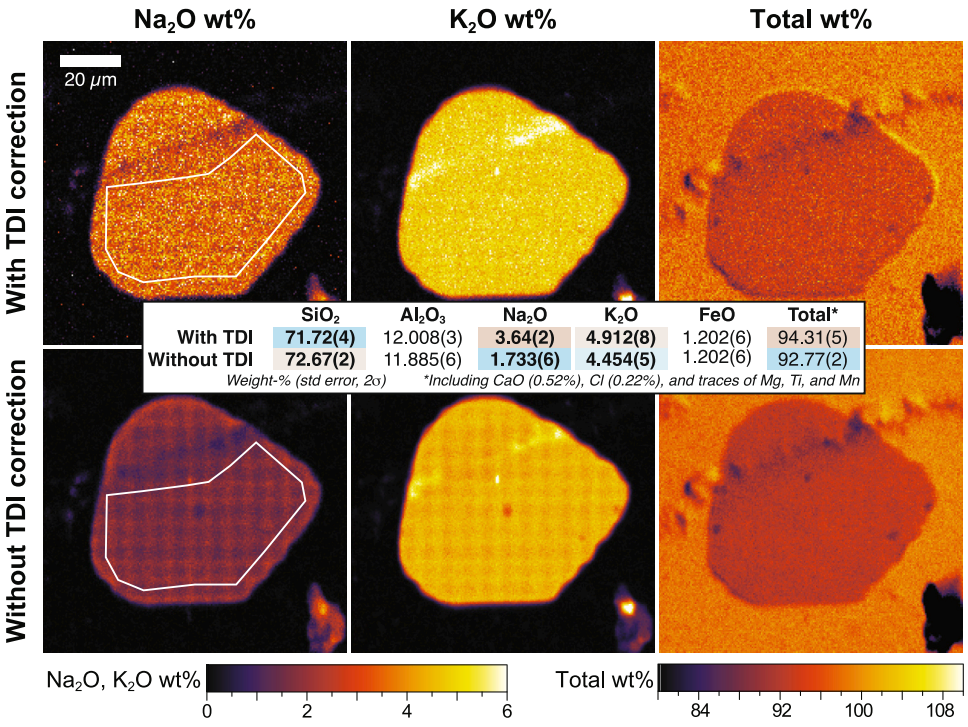

Fig. 10. Quantitative element maps for Na_2O, K_2O, and analytical total in wt% for a melt inclusion "m11" in a natural sample acquired at 15 kV, 30 nA, focused beam, 1 μm/px, and 100 ms/px, with a total of 11 TDI scanning passes. Data with and without TDI correction are compared. Averaging of pixels highlighted by the white polygon on the Na_2O wt-% map reveals a loss of the alkalis, especially Na, that correlates with an increase in Si when no TDI correction is considered. Calculated TDI correction factors reach as high as 250% and 75% for Na and K respectively. The grid pattern visible on the Na and K maps results from beam damage through stage mapping and is essentially removed when TDI corrections are applied. Matrix tables of all analyzed elements and with or without TDI are available in the Supplementary Table 4, and all processed maps are available in Supplementary Fig. 1a (no TDI) and 1b (with TDI).

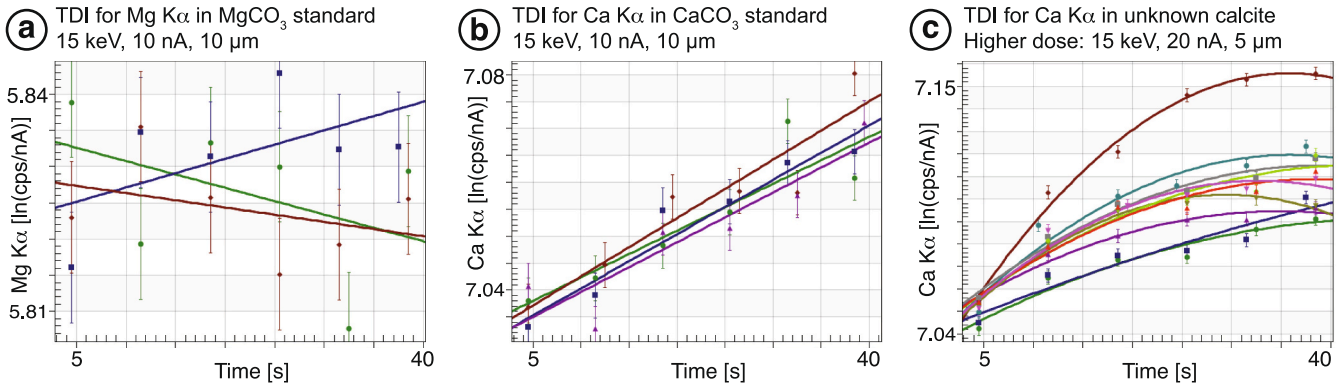

Fig. 11. TDI acquisition for (a) Mg Kα in $MgCO_3$ reference material (no TDI trend), (b) Ca Kα in $CaCO_3$ reference material (ln-linear trend), and (c) Ca Kα at higher dose in a natural Mg-bearing calcite. Analytical conditions are given above each plot. Error bars are 1σ based on counting statistics. TDI acquisition data are available in the Supplementary Table 5.

100% when CO_2 is calculated assuming stoichiometry within the matrix correction, i.e., one mole of $(CO_3)^{2-}$ for each mole of measured divalent cation.

4.3. Hydrosulfate minerals

Hydrous phases, alkali-rich phases, and sulfate can also show strong TDI effects. A dramatic example which combines all of them is the hydrosulfate series of (natro-) alunite and (natro-) jarosite $(K,Na)(Al, Fe^{3+})_3(SO_4)_2(OH)_6$. The occurrence of this mineral in altered rocks is typically in the form of 5 to 10 μm size crystal with signs of zonation at the micrometer scale in K, Na, Al, Fe, and some minor elements such as As. Sample information can be found in McCollom et al. (2013). It is so sensitive that a merely 3 s analysis of K and Na with Al and S at low current (< 2 nA) and focused beam was required on a vintage 4-spectrometer JEOL JXA-8600 at the University of Colorado Boulder to yield accurate results before irremediable beam damage and subsequent inaccurate results. As a consequence, single-point analyses yielded poor statistics, and analysis of elements <1 wt% is hard, if not impossible. TDI scanning can here again help by delivering enough counts over a longer period at higher beam density and spatial resolution, while distributing the overall energy dose over several passes. Fig. 13 shows a series of 5 passes at 50 nA and focused beam acquired on the newer 5-spectrometer JEOL JXA-8230. A strong damage is observed when the first and last passes are compared (Fig. 13a). If all passes are summed, the results are more precise (more counts), yet inaccurate in the sense that it does not depict the true chemical zoning prior to beam damage. On the contrary, more accurate results are obtained with the TDI correction. A series of

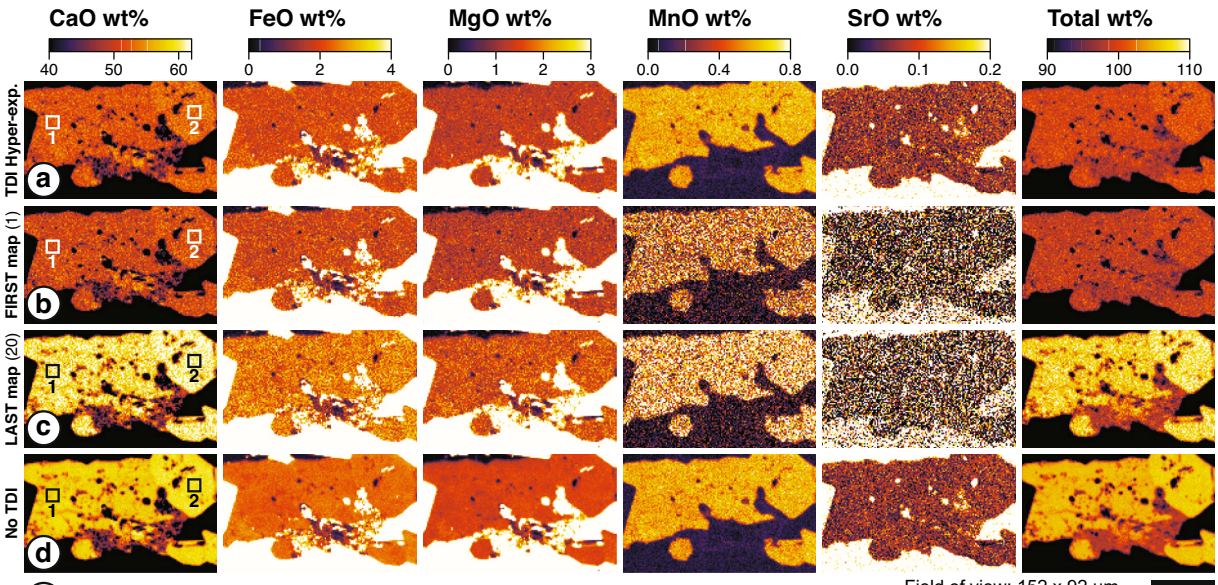

e Averages of 10x10 pixels *(see CaO maps)*

TDI?	Area #	CaO	FeO	MgO	MnO	SrO	CO_2*	Total
None	1	57.97 (8)	2.299(10)	1.466 (8)	0.572(6)	0.064(3)	*48.9*	**111.2**
Linear	1	54.01 (8)	2.052(15)	1.347(12)	0.574(6)	0.068(3)	*45.5*	**103.6**
Hyper-exp.	1	52.01(14)	1.97 (3)	1.280(22)	0.576(4)	0.070(3)	*43.8*	**99.7**
None	2	59.46 (6)	2.388(10)	1.530 (7)	0.607(6)	0.075(4)	*50.2*	**114.3**
Linear	2	55.49 (8)	2.143(14)	1.387(10)	0.610(6)	0.079(4)	*46.8*	**106.5**
Hyper-exp.	2	53.10(12)	2.09 (3)	1.362(22)	0.611(6)	0.081(4)	*44.9*	**102.1**

** by stoichiometry*

Fig. 12. Quantitative element mapping with TDI scanning in a natural Mg-bearing carbonate with trace amount of Sr obtained at 15 kV, 50 nA, focused beam, 1 µm/px, 50 ms/px, and with 20 repetitions, which sums up to 1 s per pixel. The missing CO_2 content (not shown) is calculated by stoichiometry and included in the matrix correction iteration for each map assuming a 1:3 ratio of C:O. (a) CaO, FeO, MgO, MnO, and SrO quantitative maps processed with a hyper-exponential TDI fitting on CaO (ca. -10.5% change), FeO (ca. -13%), MgO (ca. -12%), MnO (ca. +0.7%) and SrO (ca. -9%). (b,c) Comparison of quantified first and last pass to highlight the overall change in intensity. (d) Inaccurate results when ignoring the TDI trend and summing all maps. (e) Quantitative analysis obtained by averaging 10 × 10 pixels in area 1 and 2 as shown in (a), with a 1σ standard deviation given in parenthesis. Accurate and precise analysis can be extracted from the map by averaging pixels from TDI-corrected element or oxide maps, as shown with areas 1 and 2 in (a). The calculated detection limit of one pixel for SrO is ~0.21 wt%, yet the averaging of 100 pixels lowers it to 0.021 wt% (= detection limit divided by the square root of the number of repetitions), and the standard deviation is around 0.004 wt%, making the measurement of 0.070 and 0.081 wt% in area 1 and 2 respectively significant (i.e., above detection limit). Matrix tables of all analyzed elements and with or without TDI are available in the Supplementary Table 6, and all quantified oxide maps are in Supplementary Fig. 2.

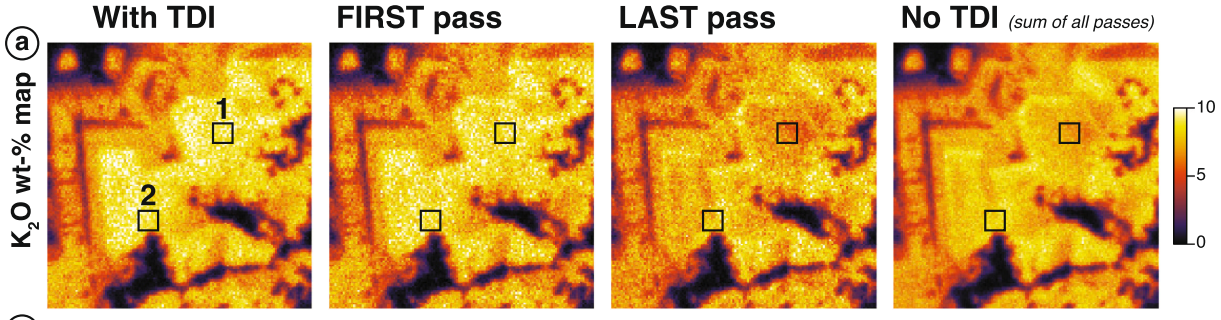

b Averages of 10x10 pixels

	K_2O	Fe_2O_3	SO_3	Al_2O_3	As_2O_3	H_2O*	Total
Area 1, aggregated	6.97 (4)	47.92(16)	33.44(15)	0.115(13)	0.064 (9)	11.03	**99.55**
Area 1, with TDI	**9.03 (6)**	46.01(24)	32.57(25)	0.106(20)	0.077(14)	10.91	**98.71**
Area 2, aggregated	8.22 (6)	44.6 (3)	31.61(26)	1.40 (8)	0.086 (8)	11.01	**96.94**
Area 2, with TDI	**8.88 (8)**	43.9 (3)	31.50(27)	1.41 (9)	0.116(13)	10.98	**96.78**

Fig. 13. (a) Example of quantitative element mapping of K_2O with TDI scanning (ln-linear correction) in a natural jarosite-alunite sample embedded in epoxy (= black pixels), compared to the first and last passes, and the summation of all 5 passes. Each single pass was obtained at 15 kV, focused beam, 50 nA, 20 ms/pixel, and at 0.5 µm/pixel resolution. Field of view is 60 µm. (b) Extraction of quantitative data by averaging 10 × 10 pixels in areas 1 and 2 highlighted in (a). More accurate data is obtained with TDI correction especially on K_2O. Additional quantitative maps of SO_3, Fe_2O_3, Al_2O_3, and analytical total are available in the Supplementary Material. A stacking of all 5 acquisitions can be seen in Supplementary Fig. 3a, along with additional softer or stronger beam conditions in Supplementary Fig. 3b-d. Matrix tables of all analyzed elements and with or without TDI are available in the Supplementary Table 7, and Supplementary Fig. 4 show all quantified element maps with or without TDI correction, and for the first and last pass.

animated GIF showing this transition is available as Supplementary Fig. 3 for this specific beam condition along with some other softer or stronger analytical conditions.

4.4. Halogens and apatite

Accurate and precise halogen measurements in apatite minerals require patience and acceptance of the limitations of the technique. As much as we try to avoid diffusion of halogens, the effect is quick and needs fast analysis with TDI to ensure accuracy. For instance, tests in multiple grains of Durango and other synthetic F-Cl apatite coated with 20 nm C reveal that damage occurs early at ~0.05 to 0.1 mJ/μm^2 and is uncorrectable beyond ~0.5 mJ/μm^2 (e.g., in one F-Cl apatite grain at multiple beam conditions, Fig. 14a-d) whereas improvement is seen with Al + C coating and an apparent maximum around 10 mJ/μm^2 (Allaz et al., 2019). The orientation effect on the apatite TDI trend is beyond the scope of this paper (e.g., Stormer et al., 1993). However, providing that TDI is considered and the total beam dose is kept below the threshold, a TDI correction can be applied to improve data accuracy especially on F-measurements (and secondly on Cl-, Ca-, and P-measurements). Comparing apatite data obtained in (Popa et al., 2021; reproduced in Fig. 14e,f) reveals a strong improvement in data clarity, which ultimately reflects the sample compositional variation rather than stochastic data due to variable beam damage effects. Limitations on trace element analysis in such minerals arise; currently our analytical setting does not show any clear TDI trend on minor and trace elements besides the halogens yet our detection limits remain >100 ppm for most "trace" elements considered (see Allaz et al., 2026). However, if stronger beam conditions and longer analysis time were to be considered, the TDI effect on minor to trace elements along with change in bremsstrahlung intensity should be expected and monitored.

4.5. Trace element analysis

Trace element studies by EPMA usually require high beam currents and long acquisition times to achieve the desired detection limits. Beam damage involving mobilization of the more volatile components (e.g., alkalis, halogens, loosely bound $[OH]^-$ or $[CO_3]^{2-}$ anion, etc.) is conventionally thought to not affect the measurement of high-Z trace elements, which are believed to be comparatively immobile (Fialin et al., 1999). However, we have observed significant TDI effects (up to 20%) in the analysis of trace elements if they are hosted in beam-sensitive materials or if an exceedingly high beam energy dose is considered (i.e., high current, small beam size, and long counting time). Low X-ray energies are more prone to TDI effects, as they are more susceptible to be absorbed (higher mass absorption coefficients), and thus more sensitive to change in matrix composition and structure. For example, we analyzed lawsonite ($CaAl_2Si_2O_7(OH)_2{\cdot}H_2O$) at conditions optimized for trace element analysis, i.e., 15 kV, 100 nA, 10 μm beam size and ~ 5 min acquisition time with TDI correction on 10 time-intervals. Despite the application of a defocused beam, this hydrated mineral phase exhibits a positive change over time of X-ray yield for Cr Kα (Fig. 15a). The averaged TDI intensity change accounts for a − 18.0 ± 0.4% correction, which is a significant impact on accuracy if left uncorrected.

While Cr is likely not migrating itself, beam damage and dehydration during analysis lead to compositional changes that alter notably the yield on characteristic X-ray and bremsstrahlung intensities. The loss of light elements increases the bremsstrahlung intensity and therefore the overall X-ray yield. All this will subsequently change the absorption effect during the analysis, resulting in the observed change in X-ray yield over time. Another example of trace element analysis is found in monazite, a light rare earth element phosphate, which is commonly used for electron microprobe dating by U-Th-Pb_{total} at the micrometer scale. Examples of TDI effects on major elements, Th and the key trace element Pb are found in Allaz et al. (2020). We here present additional data on another trace element such as Y Lα, U Mβ, and Pb Mα (Fig. 15b,c,d) that correlate with the loss of P by diffusion (not shown). This effect is not observable on minor to major elements (> 1 wt%), as the change in bremsstrahlung intensity is much less than the measurement uncertainty. It should be noted that bremsstrahlung measurement can also be affected by the TDI effect at high electron beam dose (see Fig. 5b,d of Allaz et al., 2020) and can lead to inaccuracy especially if measured after the on-peak measurement (i.e., post-damage). Such a change is revealed through the K Kα measurement in NIST glass 610, as this element is only present as an uncertified trace around 0.046 wt%. After a small apparent

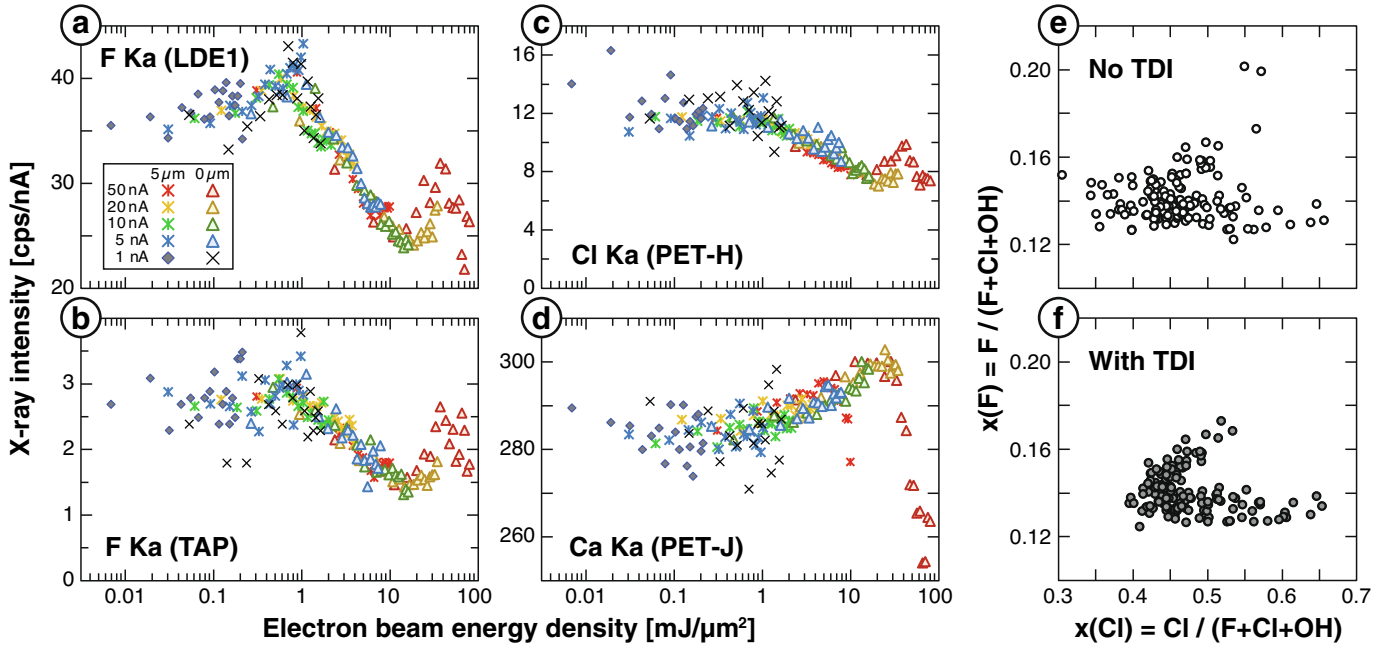

Fig. 14. (a-d) Collection of TDI acquisitions in one grain of a synthetic F-Cl apatite showing a strong TDI effect notably on F Kα (LDE1 or TAP monochromators) and also on Ca Kα (PET-J) and Cl Kα (PET-H). Data acquired at 15 kV acceleration voltage and various beam size and current. (e,f) Analytical results of F and Cl contents in natural apatite inclusions and microcrystals from Avlakia lava (e) without and (f) with TDI correction applied (see Popa et al., 2021 for details).

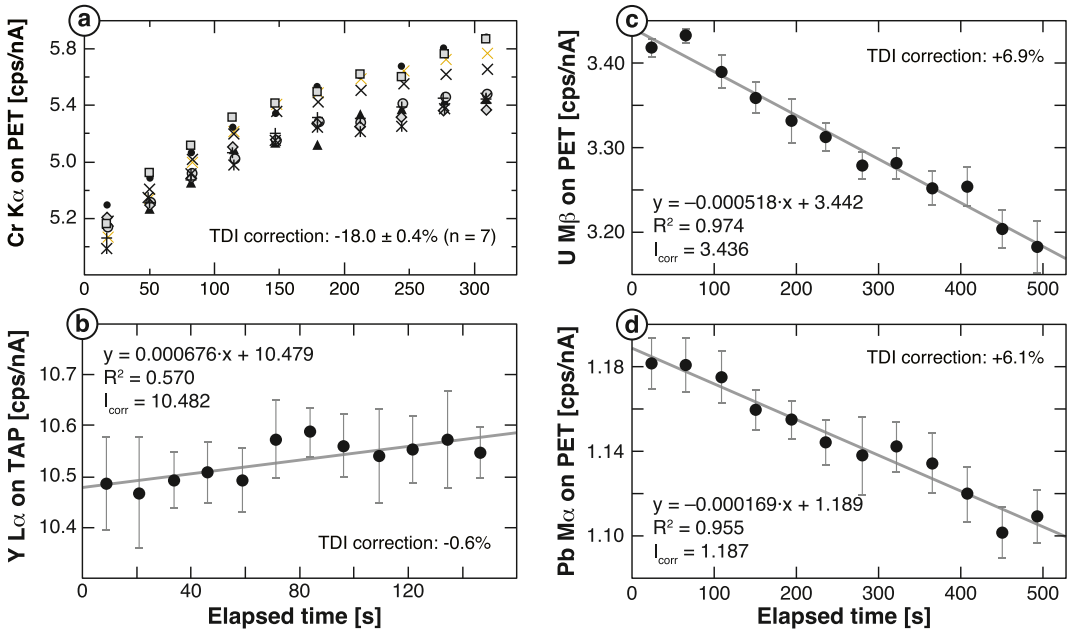

Fig. 15. Examples of TDI curves for trace elements: (a) Cr Kα in a natural lawsonite sample at 20 kV, 100 nA and 10 μm defocused beam, and (b) Y Lα, (c) U Mβ, (d) Pb Mα in Burnet monazite age reference material at 15 kV, 200 nA and focused beam (see also Allaz et al., 2020). Percentage of TDI correction is indicated on each plot, and fitting curve equation, R^2. Corrected intensity (I_{corr}) is shown for the single measurement in monazite. Numerical data are found in Supplementary Table 8.

increase, the intensity drops through beam damage at high electron dose (Fig. 4). To limit this problem, the analyst should perform a background analysis (bremsstrahlung measurement) on a first point and then move the stage to measure the peak intensity in a nearby homogeneous domain (Allaz et al., 2020) or consider the use of the MAN background correction (Donovan et al., 2016; Donovan and Tingle, 1996).

Damage to the coating can further lead to additional unexpected changes in X-ray yield due to surface charging effects appearing after volatilization of the coating at the beam impact point (Fig. 1; see also Matthews et al., 2018). Higher thermal and electrical conductivity material such as aluminum coating for monazite analysis help mitigating this effect (Allaz et al., 2020; Jercinovic et al., 2012). TDI recording has also sometimes revealed a "knickpoint" at extreme beam energy density that might suggest dramatic change on the sample or rather coating integrity as shown in natural albite (see Fig. 3 in Allaz et al., 2023).

4.6. Low kV applications

The introduction of Schottky FEG to electron microprobe has facilitated a renaissance of EPMA applications at low acceleration voltage analysis (<5 kV). At these accelerating voltages, the X-ray generation volume shrinks dramatically, facilitating analysis at very high spatial resolution. However, two hindrances are already becoming more apparent that can negatively affect accuracy. First, beam sensitivity increases as the electron energy density is focused into a smaller volume. Second, coating material and thickness take on increasing importance as this layer constitutes a larger portion of the analytical volume at these conditions. During beam irradiation, carbon coat erosion and hydrocarbon deposition occur (Hirsch et al., 1994; Buse and Kearns, 2015; Matthews et al., 2018) and can significantly impact X-ray yields of all elements owing to changing absorption through the film. In addition, the rate of carbon coat erosion and carbon contamination becomes increasingly harder to predict below 10 kV. Matthews et al. (2018) showed that a TDI correction using a linear extrapolation can be used to correct for beam irradiation effects. This paper does not investigate further low kV applications, as it would deserve another paper. However, we emphasize that routine tracking of TDI effects may be a key element in successful analysis in the low kV realm.

5. A practical guide for TDI analysis

Change of X-ray intensities from electron bombardment is a complex interplay of analytical conditions (i.e., electron beam energy density: accelerating voltage, beam current and diameter, counting times) and material and coating properties (conductivity, crystallinity, crystallographic orientation, alkali and volatile contents, etc.). There is no absolute answer for an overall correction of electron beam damage, and monitoring the X-ray yield over time is therefore necessary to achieve high accuracy. Empirical tests within the type of materials of interest are desirable to assess the maximum damage a material can suffer and still be accurately correctible with a TDI acquisition. Global assessments can be done for a group of materials of similar beam sensitivity providing that no crystallographic orientation effect is visible (e.g., rhyolitic or basaltic glasses, Na-rich feldspar, carbonate, or alkali-rich hydrosulfate).

Another common strategy to overcome problems with beam-sensitive materials is to calibrate against reference materials that shows equivalent effects under electron bombardment (Hughes et al., 2019; Kuehn et al., 2011). For very beam-sensitive glasses and in the absence of TDI correction solutions, this approach may be the only option to acquire accurate results (Kuehn et al., 2011). While this approach may not directly address the loss or gain in X-ray intensity, the concept is that any negative effects would be consistent in both standard and sample, effectively offsetting each other. When implementing this approach, it is important to adhere to specific best practices, such as ensuring that the elements on the standards are calibrated in the same order and with the same count time as the unknown samples. Additionally, when TDI corrections are applied to beam-sensitive samples in this scenario, TDI corrections should also be acquired and applied if needed for the calibration standards as well. However, this approach may not always be sufficient or feasible. This could be the case when relevant reference materials are unavailable, or when the material exhibits intricate crystallographic orientation effects for TDI, such as those seen in apatite or other beam-sensitive minerals.

In conclusion, we find that using either SC-TDI or TDI scanning yields the highest accuracy in beam-sensitive materials. The AC-TDI correction remains necessary in some materials such as fine glass shards (e.g., tephra) that are extremely beam-sensitive, yet their TDI trend remains

the same over time for a range of compositions and for an electron beam condition, and is independent of the phase orientation. Because of the varied causes of beam damage during EPMA relating to choices in analytical conditions and hardware but also the complex nature of samples, acquisition of TDI behavior should be at minimum, one part of the initial steps of method development. This approach might one day also be applied to energy dispersive spectrometry, with regular EDS scans obtained at regular intervals to monitor the loss or gain of some X-rays.

CRediT authorship contribution statement

Julien M. Allaz: Writing – original draft, Investigation, Funding acquisition, Formal analysis, Data curation. **Anette von der Handt:** Writing – original draft, Investigation, Funding acquisition, Formal analysis, Data curation. **John J. Donovan:** Writing – original draft, Software, Investigation, Formal analysis, Data curation, Conceptualization.

Declaration of competing interest

The authors declare that they have no known competing financial interests or personal relationships that could have appeared to influence the work reported in this paper.

Acknowledgements

AVDH and JMA acknowledge fundings by NSF EAR 1625422 and NSF EAR 1427626, for the purchase of the EPMA at the University of Minnesota and of Colorado Boulder (USA), respectively. JMA is thankful to ETH Zürich and D-EAPS (Switzerland) for the EPMA acquisition. JMA is grateful to Dr. Tom McCollom at the University of Colorado Boulder (USA) for providing a natural jarosite-alunite sample. JD is president of Probe Software, Inc. We thank the editor Claudia Romano and two anonymous reviewers for their valuable comments.

Appendix A. Supplementary data

Supplementary data to this article can be found online at https://doi.org/10.1016/j.chemgeo.2026.123671.

Data availability

All data and code supporting the findings of this study are available within the article and its supplementary information files.

References

Allaz, J.M., Popa, R.-G., Reusser, E., Martin, L., 2019. Electron microprobe analysis of minor and trace elements in beam sensitive materials: how far can we go? Microsc. Microanal. 25, 2312–2313. https://doi.org/10.1017/s1431927619012297.

Allaz, J.M., Jercinovic, M.J., Williams, M.L., 2020. U-Th-Pb_{TOTAL} dating of REE-phosphate by electron microprobe: review and progress. IOP Conf. Ser.: Mater. Sci. Eng. 891, 1–22. https://doi.org/10.1088/1757-899X/891/1/012001.

Allaz, J.M., Guillong, M., Tavazzani, L., Spiekermann, G., Zehnder, L., Bullock, E., DesOrmeau, J., Jercinovic, M.J., Krause, J., Marxer, F., Nachlas, W.O., Spratt, J., 2023. A new albite microanalytical reference material from Piz Beverin for Na, Al and Si determination, and the potential for new K-Feldspar reference materials. Geostand. Geoanal. Res. 47, 907–929. https://doi.org/10.1111/ggr.12515.

Allaz, J.M., Martin, L., Storck, J.-C., Ulmer, P., Reusser, E., Popa, R.-G., Chatterjee, A., Bachmann, O., 2026. Quantitative analyses by combined energy and wavelength dispersive spectrometry: the best of both worlds. Am. Mineral. https://doi.org/10.2138/am-2025-10014 (in press).

Bastin, G.F., Heijligers, H.J.M., 2004. Quantitative electron probe microanalysis of nonconducting specimens: science or art? Microsc. Microanal. 10, 733–738. https://doi.org/10.1017/S1431927604040632.

Buse, B., Kearns, S., 2015. Importance of carbon contamination in high-resolution (FEG) EPMA of silicate minerals. Microsc. Microanal. 21, 594–605. https://doi.org/10.1017/S1431927615000288.

Chantler, C.T., Olsen, K., Dragoset, R.A., Chang, J., Kishore, A.R., Kotochigova, S.A., Zucker, D.S., 2005. X-Ray Form Factor, Attenuation and Scattering Tables (Version 2.1). [Online] [WWW Document]. National Institute of Standards and Technology, Gaithersburg, MD. URL. http://physics.nist.gov/ffast (accessed 5.26.26).

Donovan, J.J., Tingle, T.N., 1996. An improved mean atomic number background correction for quantitative microanalysis. J. Microsc. Microanal. 2, 1–7.

Donovan, J.J., Snyder, D.A., Rivers, M.L., 1993. An improved interference correction for trace element analysis. Microbeam Anal. 2, 23–28.

Donovan, J.J., Lowers, H.A., Rusk, B.G., 2011. Improved electron probe microanalysis of trace elements in quartz. Am. Mineral. 96, 274–282. https://doi.org/10.2138/am.2011.3631.

Donovan, J.J., Moy, A., von der Handt, A., Gainsforth, Z., Maner, J.L., Nachlas, W., Fournelle, J., 2023. A new method for dead time calibration and a new expression for correction of WDS intensities for microanalysis. Microsc. Microanal. 29, 1096–1110. https://doi.org/10.1093/micmic/ozad050.

Donovan, J.J., Singer, J.W., Armstrong, J.T., 2016. A new EPMA method for fast trace element analysis in simple matrices. Am. Mineral. 101, 1839–1853. https://doi.org/10.2138/am-2016-5628.

Donovan, J.J., Allaz, J.M., von der Handt, A., Seward, G.G.E., Neill, O., Goemann, K., Chouinard, J., Carpenter, P.K., 2021. Quantitative WDS compositional mapping using the electron microprobe. Am. Mineral. 106, 1717–1735. https://doi.org/10.2138/am-2021-7739.

Egerton, R.F., Crozier, P.A., Rice, P., 1987. Electron energy-loss spectroscopy and chemical change. Ultramicroscopy 23, 305–312.

Egerton, R.F., Li, P., Malac, M., 2004. Radiation damage in the TEM and SEM. Micron 35, 399–409. https://doi.org/10.1016/j.micron.2004.02.003.

Estour, H., 1971. Observation sur la modification de verres par le faisceau électronique d'une microsonde. Verres Réfractaires 25, 11–17.

Fakhfakh, S., Elsafi, B., Fakhfakh, Z., Jbara, O., 2012a. Study of temperature effects on the conduction and trapping of charges in the alkali-silicate glass under electron beam irradiation. Appl. Surf. Sci. 258, 2324–2331. https://doi.org/10.1016/j.apsusc.2011.10.007.

Fakhfakh, S., Jbara, O., Rondot, S., Hadjadj, A., Fakhfakh, Z., 2012b. Experimental characterisation of charge distribution and transport in electron irradiated PMMA. J. Non-Cryst. Solids 358, 1157–1164. https://doi.org/10.1016/j.jnoncrysol.2012.02.015.

Fialin, M., Rémy, H., Richard, C., Wagner, C., 1999. Trace element analysis with the electron microprobe: new data and perspectives. Am. Mineral. 84, 70–77.

Gedeon, O., Jurek, K., 2004. Relaxation of alkali glass exposed to an electron beam. In: Microchimica Acta. Springer New York, pp. 49–52. https://doi.org/10.1007/s00604-003-0125-y.

Gedeon, O., Hulínský, V., Jurek, K., 1998. The analytical signal in EPMA and the influence of the electric field created by the primary beam. In: Modern Developments and Applications in Microbeam Analysis. Springer Vienna, Vienna, pp. 301–305. https://doi.org/10.1007/978-3-7091-7506-4_40.

Gedeon, O., Hulínský, V., Jurek, K., 2000. Microanalysis of glass containing alkali ions. Microchim. Acta 132, 505–510. https://doi.org/10.1007/s006040050050.

Gedeon, O., Zemek, J., Jurek, K., 2008. Changes in alkali-silicate glasses induced with electron irradiation. J. Non-Cryst. Solids 354, 1169–1171. https://doi.org/10.1016/j.jnoncrysol.2006.12.125.

Goldoff, B., Webster, J.D., Harlov, D.E., 2012. Characterization of fluor-chlorapatites by electron probe microanalysis with a focus on time-dependent intensity variation of halogens. Am. Mineral. 97, 1103–1115. https://doi.org/10.2138/am.2012.3812.

Hirsch, P., Kässens, M., Püttmann, M., Reimer, L., 1994. Contamination in a scanning electron microscope and the influence of specimen cooling. Scanning 16, 101–110. https://doi.org/10.1002/sca.4950160207.

Holá, M., Ondráček, J., Nováková, H., Vojtíšek-Lom, M., Hadravová, R., Kanický, V., 2018. The influence of material properties on highly time resolved particle formation for nanosecond laser ablation. Spectrochim. Acta Part B At. Spectrosc. 148, 193–204. https://doi.org/10.1016/j.sab.2018.07.001.

Hughes, E.C., Buse, B., Kearns, S.L., Blundy, J.D., Kilgour, G., Mader, H.M., 2019. Low analytical totals in EPMA of hydrous silicate glass due to sub-surface charging: obtaining accurate volatiles by difference. Chem. Geol. 505, 48–56. https://doi.org/10.1016/j.chemgeo.2018.11.015.

Hughes, E.C., Buse, B., Kearns, S.L., Brooker, R.A., Di Genova, D., Kilgour, G., Mader, H.M., Blundy, J.D., 2020. The microanalysis of iron and Sulphur oxidation states in silicate glass - Understanding the effects of beam damage. In: IOP Conference Series: Materials Science and Engineering. IOP Publishing Ltd. https://doi.org/10.1088/1757-899X/891/1/012014.

Jbara, O., Portron, B., Mouze, D., Cazaux, J., 1997. Electron probe microanalysis of insulating oxides: Monte Carlo simulations. X-Ray Spectrom. 26, 291–302. https://doi.org/10.1002/(SICI)1097-4539(199709)26:5<291::AID-XRS226>3.0.CO;2-X.

Jercinovic, M.J., Williams, M.L., Allaz, J., Donovan, J.J., 2012. Trace analysis in EPMA. IOP Conf. Ser.: Mater. Sci. Eng. 32, 1–22. https://doi.org/10.1088/1757-899X/32/1/012012.

Jiang, N., 2016. Beam damage by the induced electric field in transmission electron microscopy. Micron 83, 79–92. https://doi.org/10.1016/j.micron.2016.02.007.

Jiang, N., Spence, J.C.H., 2011. In situ EELS study of dehydration of Al(OH)3 by electron beam irradiation. Ultramicroscopy 111, 860–864. https://doi.org/10.1016/j.ultramic.2010.11.004.

Jurek, K., Gedeon, O., Hulínský, V., 1998. Potassium migration in silica glass during electron beam irradiation. In: Modern Developments and Applications in Microbeam Analysis. Springer Vienna, Vienna, pp. 269–272. https://doi.org/10.1007/978-3-7091-7506-4_36.

Kearns, S.L., Buse, B., 2016. Low voltage FEG-EPMA in Earth sciences–problems and solutions for analysis of unstable materials. Microsc. Microanal. 22, 416–417. https://doi.org/10.1017/S1431927616002932.

Kearns, S.L., Steen, N., Erlund, E., 2002. Electronprobe microanalysis of volcanic glass at cryogenic temperatures. Microsc. Microanal. 8, 1562–1563. https://doi.org/10.1017/S1431927602107562.

Kearns, S., Buse, B., Wade, J., 2014. Mitigating thermal beam damage with metallic coats in low voltage FEG-EPMA of geological materials. Microsc. Microanal. 20, 740–741. https://doi.org/10.1017/S143192761400542X.

Koepke, J., Feig, S.T., Snow, J., Freise, M., 2004. Petrogenesis of oceanic plagiogranites by partial melting of gabbros: an experimental study. Contrib. Mineral. Petrol. 146, 414–432. https://doi.org/10.1007/s00410-003-0511-9.

Kuehn, S.C., Froese, D.G., Shane, P.A.R., 2011. The INTAV intercomparison of electron-beam microanalysis of glass by tephrochronology laboratories: results and recommendations. Quat. Int. 246, 19–47. https://doi.org/10.1016/j.quaint.2011.08.022.

Lane, S.J., Dalton, J.A., 1994. Electron microprobe analysis of geological carbonates. Am. Mineral. 79, 745–749.

Matthews, M.B., Kearns, S.L., Buse, B., 2018. Electron beam-induced carbon erosion and the impact on electron probe microanalysis. Microsc. Microanal. 24, 612–622. https://doi.org/10.1017/S1431927618015398.

McCollom, T.M., Robbins, M., Moskowitz, B., Berquō, T.S., Jöns, N., Hynek, B.M., 2013. Experimental study of acid-sulfate alteration of basalt and implications for sulfate deposits on Mars. J. Geophys. Res. Planets 118, 577–614. https://doi.org/10.1002/jgre.20044.

Morgan, G.B., London, D., 1996. Optimizing the electron microprobe analysis of hydrous alkali aluminosilicate glasses. Am. Mineral. 81, 1176–1185. https://doi.org/10.2138/am-1996-9-1016.

Morgan, G.B., London, D., 2005. Effect of current density on the electron microprobe analysis of alkali aluminosilicate glasses. Am. Mineral. 90, 1131–1138. https://doi.org/10.2138/am.2005.1769.

Nielsen, C.H., Sigurdsson, H., 1981. Quantitative methods for electron microprobe analysis of sodium in natural and synthetic glasses. Am. Mineral. 66, 547–552.

Popa, R.G., Tollan, P., Bachmann, O., Schenker, V., Ellis, B., Allaz, J.M., 2021. Water exsolution in the magma chamber favors effusive eruptions: application of Cl-F partitioning behavior at the Nisyros-Yali volcanic area. Chem. Geol. 570. https://doi.org/10.1016/j.chemgeo.2021.120170.

Reimer, L., 1998. Scanning Electron Microscopy, Optical Sciences. Springer-Verlag Berlin Heidelberg GmbH, p. 538.

Saunders, K., Buse, B., Kilburn, M.R., Kearns, S., Blundy, J., 2014. Nanoscale characterisation of crystal zoning. Chem. Geol. 364, 20–32. https://doi.org/10.1016/j.chemgeo.2013.11.019.

Spray, J.G., Rae, D.A., 1995. Quantitative electron-microprobe analysis of alkali silicate glasses: a review and user guide. Can. Mineral. 33, 323–332.

Stormer, J.C., Pierson, M.L., Tacker, R.C., 1993. Variation of F and Cl X-ray intensity due to anisotropic diffusion in apatite during electron microprobe analysis. Am. Mineral. 78, 641–648.

Vassamillet, L.F., Caldwell, V.E., 1969. Electron-probe microanalysis of alkali metals in glasses. J. Appl. Phys. 40, 1637–1643. https://doi.org/10.1063/1.1657825.

Vicenzi, E.P., Eggins, S., Logan, A., Wysoczanski, R., 2002. Microbeam characterization of corning archeological reference glasses: new additions to the Smithsonian Microbeam Standard collection. J. Res. Natl. Inst. Stand. Technol. 107, 719–727.

Witter, J.B., Kuehner, S.M., 2004. A simple empirical method for high-quality electron microprobe analysis of fluorine at trace levels in Fe-bearing minerals and glasses. Am. Mineral. 89, 57–63. https://doi.org/10.2138/am-2004-0108.

Worobiec, A., De Hoog, J., Osán, J.A., Szalóki, I., Ro, C.U., Van Grieken, R., 2003. Thermal stability of beam sensitive atmospheric aerosol particles in electron probe microanalysis at liquid nitrogen temperature. Spectrochim. Acta Part B At. Spectrosc. 58, 479–496. https://doi.org/10.1016/S0584-8547(03)00013-2.